AIAA JOURNAL
Vol. 47, No. 1, January 2009

Direct and Large-Eddy Simulations of Merging in Corotating Vortex System

L. Nybelen* and R. Paoli†
European Center for Research and Advanced Training in Scientific Computation, 31057 Toulouse Cedex 1, France

DOI: 10.2514/1.38026

Direct and large-eddy simulations were used to study the process of the merging of a corotating vortex system, an important topic of aircraft wake dynamics. A simplified configuration was chosen, consisting of a couple of corotating, symmetrical vortices whose initial distribution of vorticity obeys an analytical law. The Lamb–Oseen model and the two-scale VM2 model by Fabre and Jacquin were used to initialize the simulations in the two-dimensional (stable) and three-dimensional (unstable) cases, for Reynolds numbers based on circulation ranging from $Re_\Gamma = 7.5 \times 10^2$ to 2.4×10^5, and for various initial ratios a_0/b_0 between the vortex core size and vortex spacing. In all cases, the onset of merging is associated with an exchange of vorticity between vortices; in the unstable cases this process is faster as it is triggered by a short-wave elliptical instability whose wavelength depends on the actual ratio a/b at the beginning of the linear regime, which may be relevant, for example, for the development of wake control strategies. The structure of the final merged vortex is characterized by a two-scale azimuthal velocity profile, with a steeper intermediate power-law region in the case of unstable merging compared with stable merging.

I. Introduction

THE merging of two- and three-dimensional vortices occurs in a number of fundamental processes of fluid mechanics, such as two-dimensional [1] and three-dimensional [2] turbulence, as well as in meteorology and in geophysical flows [3]. Merging plays a major role in the formation of aircraft trailing vortices. In the initial stages of its formation, the wake of an aircraft is a complex vortex system composed of multiple interacting counter-rotating and corotating vortices that are generated by the roll-up of the vorticity sheet shed by the wing and its components like flaps, spoilers, and engine nacelles [4,5]. All these vortices merge into a pair of coherent counter-rotating vortices and represent a hazard for following aircraft, in particular during takeoff and landing phases (e.g., the classical review by Spalart [6] and the recent special issue by Crouch and Jacquin [7] and references therein). This motivated the extensive research that has been conducted both in the U.S. and Europe to characterize the structure of such vortices, to model their evolution, and to develop concepts to accelerate their decay [8–14]. In particular, Holzäpfel [12,14] recently proposed a probabilistic model that predicts in real time the decay of the wake vortex as a function of aircraft and environmental parameters (such as wind, atmospheric turbulence, and stratification). All these models were assessed using observation data from field deployment at the international airports of Memphis and Dallas and from the WakeOP and WakeToul experimental campaigns during EU-funded projects C-Wake and Awiator, at Oberpfaffenhofen and Tarbes airports, respectively. The present study focuses on one aspect of the problem, namely the process of the merging of two corotating vortices in the extended near-field of the wake (i.e., one to ten wingspans behind the aircraft). This occurs, for example, in high-lift wing configurations where the two vortices are generated at the wing-tip and flap positions, respectively. The experimental work by Cerretelli and Williamson [15] first showed that at a low Reynolds number, vortex merging can be represented in four stages: a first diffusion stage, a convective stage, a second diffusion stage, and an axisymmetrization stage (the main features of each phase will be discussed in detail in the analysis of the numerical simulations in Sec. III.C). They also found that the onset of merging is related to the generation of an antisymmetric vorticity field that brings the two vortices together and observed that the final merging time depends on the Reynolds number as well as the initial ratio a_0/b_0 between the vortex core size a and spacing b. Meunier et al. [16] found that a pair of two-dimensional corotating vortices start to merge when this characteristic ration exceeds a critical threshold $(a/b)_c \approx 0.22$. These results were later on confirmed by Leweke et al. [17] both experimentally and numerically. In real aircraft wakes the initial ratio a_0/b_0 of the primary corotating vortices is often smaller than $(a/b)_c$; however, the size of the vortex core increases during the roll-up of the vortex sheet, although the interaction with remnants of the vortex sheet and the multiple vortices present in the wake reduce the vortex spacing. This increases the ratio a/b and ultimately leads to the merging of the vortices. The influence of the Reynolds number on the two-dimensional merging was studied in detail by Ferreira de Sousa and Pereira [18] by means of direct numerical simulation (DNS). Although limited to low Reynolds numbers and two-dimensional flows, their analysis focused on the third stage of merging, which consists of a rotational movement coupled with a diffusion process. In particular, they observed a merging in two stages for Reynolds numbers less than 5.0×10^2. Orlandi [19] recently investigated the dependence of three-dimensional merging on Reynolds numbers and the characteristic ratio a/b using direct simulations. He showed that merging is associated with a large increase in pressure extremum and that the complex feature of three-dimensional merging (compared with the two-dimensional case) can be related to the axial disturbances imposed to the two vortices.

It is known that, depending on the initial spacing and core size, two corotating vortices can be unstable due to the strain field that each vortex exerts on the other. (See the classical work by Moore and Saffmann [20] and the review by Kerswell [21] and references therein for various applications in science and engineering). The resulting "elliptical" instability is characterized by a three-dimensional sinusoidal deformation of the core and a wavelength of the order of the vortex core size. In the context of aircraft wakes, this is usually referred to as short-wave instability to distinguish from long-wave or Crow [22] instability whose wavelength is of the order of the vortex spacing. The elliptical instability was observed numerically and experimentally both in counter-rotating [23,24] and

Received 11 April 2008; accepted for publication 22 September 2008.

*Ph.D. Student, 42 Avenue Gaspard Coriolis; nybelen@cerfacs.fr.
†Senior Researcher, 42 Avenue Gaspard Coriolis; paoli@cerfacs.fr. Member AIAA.

corotating vortices [25]. Le Dizès and Laporte [26] derived an analytical relation that predicts the growth rate of the elliptical instability during the linear regime of its evolution as a function of a_0/b_0 and the Reynolds number. This theoretical analysis was based on Gaussian distribution of the initial vorticity field and was supported by direct and large-eddy simulations.

Meunier et al. [27] recently reviewed the physics of vortex merging and identified some key issues that deserve further investigation, both from a modeling and a computational point of view: 1) the effects of initial non-Gaussian vortex profiles in determining the characteristics of the merging process, 2) the effects of nonsymmetric vortex profiles, and 3) the effects of axial velocity deficit. In this study we aim at elucidating the first of these issues using direct and large-eddy simulations of trailing vortices. In particular, we are interested in evaluating the impact of vortex modeling on the development and wave selection of the elliptical instability (which is an important issue in aircraft wakes where short- and long-wavelength instabilities may occur together) [23], as well as on the structure of the final merged vortex. The first model we analyze is the classical, one-scale (Gaussian) Lamb–Oseen (LO) vortex model, which is used for validation and comparison with previous studies [17,26]; the second model is the VM2 two-scale model proposed by Fabre and Jacquin [28] that is supposed to model the roll-up of the vortex sheet [29,30] and was found to best fit the vortex profile in the extended near-field of a model-scale wake [30].

The paper is organized as follows. The governing equations, the LES (large-eddy simulation) model, and the numerical method are described in Sec. II. The results of the simulations are presented in Sec. III. The vortex models used to initialize the simulations and the computational set-up are detailed in Sec. III.A and III.B, respectively; and the numerical results of stable merging are presented in Sec. III.C and are compared with analytical predictions and experimental results available in the literature. The analysis of three-dimensional merging and its relation with the development of elliptical instability are presented in Sec. III.D. Conclusions are given in Sec. IV.

II. Governing Equations and Numerical Model

A. Governing Equations

In conservative form, the transport equations of a compressible gas read

$$\frac{\partial \rho}{\partial t} + \nabla \cdot (\rho \mathbf{u}) = 0 \tag{1}$$

$$\frac{\partial (\rho \mathbf{u})}{\partial t} + \nabla \cdot (\rho \mathbf{u} \otimes \mathbf{u} + p\mathbf{I}) - \nabla \cdot \mathbf{T} = 0 \tag{2}$$

$$\frac{\partial (\rho E)}{\partial t} + \nabla \cdot (\rho H \mathbf{u}) - \nabla \cdot (\mathbf{T}\mathbf{u}) + \nabla \cdot \mathbf{q} = 0 \tag{3}$$

where ρ is the gas density and $\mathbf{u}$ is the velocity vector. The total energy E is the sum of internal energy $e = C_v T$ and kinetic energy $K \equiv 1/2\|\mathbf{u}\|^2$: $E = C_v T + K$ where T is the temperature, R is the gas constant for air, $C_v = R/(\gamma - 1)$ and $C_p = C_v + R$ are, respectively, the specific heats at constant volume and constant pressure, and $\gamma = C_p/C_v = 1.4$ is the ratio of specific heats. Temperature and pressure are related through the equation of state $p = \rho RT$, and total enthalpy is defined by $H = E + p/\rho = C_p T + K$. The stress tensor is given by $\mathbf{T} = 2\mu(\mathbf{S} - 1/3\nabla \cdot \mathbf{u}\,\mathbf{I})$ where the strain rate tensor $\mathbf{S} = \frac{1}{2}(\nabla \mathbf{u} + \nabla \mathbf{u}^T)$ is the symmetric part of the velocity gradient and μ is the dynamic viscosity given by Sutherland's law, $\mu/\mu_{\text{ref}} = (T/T_{\text{ref}})^{0.76}$. The heat fluxes are given by Fourier's law, $\mathbf{q} = -\lambda \nabla T$ where the thermal conductivity $\lambda = \mu C_p/\Pr$ is constructed by setting the molecular Prandtl number to $\Pr = 0.75$, which is a typical value in the atmosphere [31].

B. Large-Eddy Simulation Approach and Subgrid Scale Model Description

In the LES approach Eqs. (1–3) are filtered spatially, so that any variable $\phi(x)$ is decomposed into a resolved (or large-scale) part $\overline{\phi(x)}$ and a nonresolved (or subgrid-scale) part $\phi''(x)$, with $\phi(x) = \overline{\phi(x)} + \phi''(x)$. This procedure may be obtained by a convolution integral of the variable with any filter function depending on a filter width Δ (in practice, the size of the computational cell Δ_x). In compressible flows, the large-scale filtered variables are usually recast in terms of Favre-filtered quantities defined by $\tilde{\phi} = \overline{\rho\phi}/\bar{\rho}$ with $\phi(x) = \tilde{\phi}(x) + \phi'(x)$. Applying the Favre filter to Eqs. (1–3) yields

$$\frac{\partial \bar{\rho}}{\partial t} + \nabla \cdot (\bar{\rho}\,\tilde{\mathbf{u}}) = 0 \tag{4}$$

$$\frac{\partial (\bar{\rho}\,\tilde{\mathbf{u}})}{\partial t} + \nabla \cdot (\bar{\rho}\,\tilde{\mathbf{u}} \otimes \tilde{\mathbf{u}} + \bar{p}\mathbf{I}) - \nabla \cdot \tilde{\mathbf{T}} = -\nabla \cdot \mathbf{T}_{\text{sgs}} \tag{5}$$

$$\frac{\partial (\bar{\rho}\tilde{E})}{\partial t} + \nabla \cdot (\bar{\rho}\tilde{H}\,\tilde{\mathbf{u}}) - \nabla \cdot (\tilde{\mathbf{T}}\,\tilde{\mathbf{u}}) + \nabla \cdot \tilde{\mathbf{q}} = \nabla \cdot \mathbf{q}_{\text{sgs}} - \nabla \cdot \mathbf{k}_{\text{sgs}} \tag{6}$$

where the classical assumptions by Erlebacher et al. [32] have been made: 1) the Favre-filtered shear stresses and the heat and scalar fluxes are identified with their filtered counterparts, and 2) the subgrid-scale (SGS) correlations involving fluctuations of molecular viscosity are neglected (i.e. $\bar{\mathbf{T}} \simeq \tilde{\mathbf{T}} \simeq 2\bar{\mu}(\tilde{\mathbf{S}} - 1/3\nabla \cdot \tilde{\mathbf{u}}\,\mathbf{I})$; $\tilde{\mathbf{q}} \simeq \bar{\mathbf{q}} \simeq -\bar{\mu}C_p/\Pr\,\nabla\tilde{T}$). The Favre-filtered equation of state becomes $\bar{p} = \bar{\rho}R\tilde{T}$ so that the left-hand side of Eqs. (4–6) only contains resolved quantities. On the other hand, the unresolved SGS inviscid fluxes in the right-hand side $\mathbf{T}_{\text{sgs}} \equiv \rho\widetilde{\mathbf{u} \otimes \mathbf{u}} - \bar{\rho}\,\tilde{\mathbf{u}} \otimes \tilde{\mathbf{u}}$; $\mathbf{k}_{\text{sgs}} \equiv \rho\widetilde{K\mathbf{u}} - \bar{\rho}\,\tilde{K}\,\tilde{\mathbf{u}}$, and $\mathbf{q}_{\text{sgs}} \equiv \rho\widetilde{C_p T\mathbf{u}} - \bar{\rho}C_p\tilde{T}\,\tilde{\mathbf{u}}$ are modeled through eddy viscosity concepts:

$$\mathbf{T}_{\text{sgs}} - \frac{\text{tr}(\mathbf{T}_{\text{sgs}})}{3}\mathbf{I} = -2\mu_{\text{sgs}}\left(\tilde{\mathbf{S}} - \frac{\nabla \cdot \tilde{\mathbf{u}}}{3}\mathbf{I}\right) \tag{7}$$

$$\mathbf{k}_{\text{sgs}} = \mathbf{T}_{\text{sgs}}\tilde{\mathbf{u}} \tag{8}$$

$$\mathbf{q}_{\text{sgs}} = -\frac{\mu_{\text{sgs}}C_p}{\Pr_{\text{sgs}}}\nabla\Theta \tag{9}$$

where μ_{sgs} is the SGS dynamic viscosity and $\Theta = \tilde{T} - 1/2\bar{\rho}C_v\text{tr}(\mathbf{T}_{\text{sgs}})$ is the modified temperature introduced by Lesieur and Comte [33] with $\text{tr}(\mathbf{T}_{\text{sgs}})$ the trace of the SGS stress tensor. The latter is also an unresolved term and should be modeled as it was done by Yoshizawa [34]. However, as shown by Ng and Erlebacher [35] and Lesieur and Comte [33], $\text{tr}(\mathbf{T}_{\text{sgs}}) \sim M_{\text{sgs}}^2$, with M_{sgs} the SGS Mach number that is generally negligible in weakly compressible flows as those studied in this work. Thus, we assume $\Theta = \tilde{T}$. The turbulent Prandtl and Schmidt numbers $\Pr_{\text{sgs}}$ and Sc_{sgs} are set equal to 0.419 as suggested by Gerz and Holzäpfel [36] and in accordance with the results by Moin et al. [37] and Pitsch et al. [38] for turbulent shear flows. The SGS viscosity model is based on the structure function model developed by Métais and Lesieur [39] in spectral space and then transposed into physical space by Ducros et al. [40]. The structure function is defined by

$$\bar{F}_2(\mathbf{x}, \Delta, t) = \langle \|\tilde{\mathbf{u}}(\mathbf{x} + \mathbf{r}, t) - \tilde{\mathbf{u}}(\mathbf{x}, t)\|^2 \rangle_{\|\mathbf{r}\| = \Delta} \tag{10}$$

where $\Delta = (\Delta_x \Delta_y \Delta_z)^{1/3}$ is the cutoff length and $\langle\,\rangle$ denotes spatial averaging over a sphere of radius Δ. As the information brought by the model in Eq. (10) is local in space, it leads to a poor estimation of the kinetic energy at the cutoff wavelength, which can be improved by a suitable filtering to remove the influence of large scales on SGS

viscosity. The procedure defined by Ducros et al. [40] consists of applying a discrete Laplacian high-pass filter to the velocity field before calculating the structure function. The resulting filtered structure function model yields for the turbulent viscosity

$$\mu_{\text{sgs}} = \bar{\rho}\nu_{\text{sgs}} = \bar{\rho}\alpha^{(n)}\Delta\sqrt{\bar{F}_2{}^{(n)}(\mathbf{x}, \Delta, t)} \tag{11}$$

where the superscript n indicates that the filter has been applied n times. The optimum values obtained by Ducros et al. [40] are $n = 3$ and $\alpha^{(3)} = 0.00084$. The formulation defined by Eqs. (7–11) ensures that the SGS viscosity vanishes when there is no energy at the cutoff wavelength, which is crucial for the simulation of transitional flows, as shown in comparative analysis of SGS models for the LES of trailing vortices [41]. For example, large-eddy simulations of the elliptical stability of a vortex pair by Le Dizès and Laporte [26] showed that the model correctly predicts the evolution of the vortex core radius and the transition to turbulence at a high Reynolds number.

C. Nondimensionalization

The transport Eqs. (1–6) supplemented by the model (7–11) are solved in nondimensional form using reference variables that univocally identify a reference or infinite state: length l_{ref}, density $\rho_{\text{ref}} \equiv \rho_\infty$, temperature $T_{\text{ref}} \equiv T_\infty/(\gamma - 1)$, speed of sound $a_{\text{ref}} \equiv a_\infty = \sqrt{\gamma R T_\infty}$, pressure $p_{\text{ref}} \equiv p_\infty/\gamma$, dynamic viscosity $\mu_{\text{ref}} \equiv \mu_\infty$, and specific heat $C_{p,\text{ref}} \equiv C_{p_\infty}$. Inserting Eqs. (7–9) into Eqs. (4–6) and defining the Reynolds number based on reference variables $\text{Re} = \rho_{\text{ref}} a_{\text{ref}} l_{\text{ref}}/\mu_{\text{ref}}$ finally yields (symbol $+$ denotes nondimensional variables)

$$\frac{\partial \bar{\rho}^+}{\partial t^+} + \nabla^+ \cdot (\bar{\rho}^+ \tilde{\mathbf{u}}^+) = 0 \tag{12}$$

$$\frac{\partial(\bar{\rho}^+ \tilde{\mathbf{u}}^+)}{\partial t} + \nabla^+ \cdot (\bar{\rho}^+ \tilde{\mathbf{u}}^+ \otimes \tilde{\mathbf{u}}^+ + \bar{p}^+ \mathbf{I}) = \frac{1}{Re}\nabla^+ \cdot \left[2(\bar{\mu}^+ + \mu^+_{\text{sgs}})\left(\tilde{\mathbf{S}}^+ - \frac{\nabla^+ \cdot \tilde{\mathbf{u}}^+}{3}\mathbf{I}\right)\right] \tag{13}$$

$$\begin{aligned}\frac{\partial(\bar{\rho}^+ \tilde{E}^+)}{\partial t} + \nabla^+ \cdot (\bar{\rho}^+ \tilde{H}^+ \tilde{\mathbf{u}}^+) &= \frac{1}{Re}\nabla^+ \cdot \left[2(\bar{\mu}^+ + \mu^+_{\text{sgs}})\left(\tilde{\mathbf{S}}^+ - \frac{\nabla^+ \cdot \tilde{\mathbf{u}}^+}{3}\mathbf{I}\right)\tilde{\mathbf{u}}^+\right] \\ &+ \frac{1}{Re}\nabla^+ \cdot \left[\left(\frac{\bar{\mu}^+}{\text{Pr}} + \frac{\mu^+_{\text{sgs}}}{\text{Pr}_{\text{sgs}}}\right) C_p^+ \nabla^+ \tilde{T}^+\right]\end{aligned} \tag{14}$$

Note that the resulting set of Eqs. (12–14) are equivalent to the unfiltered compressible Navier–Stokes equations with the formal substitutions $\mu \to \bar{\mu} + \mu_{\text{sgs}}$ and $\lambda/C_p \equiv \mu/\text{Pr} \to \bar{\mu}/\text{Pr} + \mu_{\text{sgs}}/\text{Pr}_{\text{sgs}}$.

D. Numerical Method

The nondimensional transport Eqs. (12–14) are discretized on collocated meshes with nonuniform grid spacing using a three-dimensional, finite differences Navier–Stokes solver [42,43]. The code has been previously used and validated for temporal simulations of wake flows including corotating [26] and counter-rotating [24,44] vortices, jet/vortex interactions [45,46], and vortex bursting [47]. The spatial derivatives are computed using the sixth-order compact scheme by Lele [48] with modified coefficients to take into account the exact metrics of the mesh [43]. As shown by Gamet et al. [43], the precision of the scheme reduces to fourth (third) order for the approximation of the first (second) derivative on stretched grids. In this work the mesh is enclosed in such a way that the vortex system is contained in a core region with uniform grid spacing and is stretched away using a geometric law (see Fig. 1). This ensures that the scheme is still formally sixth-order accurate in the uniform region of interest where one needs the highest precision to resolve the vortex instability and turbulence. On the other hand, mesh stretching ensures that the boundaries of the domain are sufficiently far to reduce the influence of boundary conditions. We use symmetry boundary conditions in the transversal plane containing the vortices (this avoids inflow of spurious waves into the computational domain) [49], and periodic boundary conditions are used in the axial direction as usually employed in temporal simulations. Finally, time integration is performed by means of a low-storage third-order Runge–Kutta method. To ensure the numerical stability, the Courant–Friedrichs–Lewy number is fixed to $\text{CFL} = 0.5$. The peak Mach number of a typical simulation is about 0.2, which shows that the flow is weakly compressible (as it is usually the case in wake vortices). Although the use of compressible equations imposes more severe time-step restriction in this case compared with their incompressible counterpart, yet it allows a wider range of applications (such as the interaction of vortices with exhaust jets) and has been retained throughout our research work on aircraft wake phenomena.

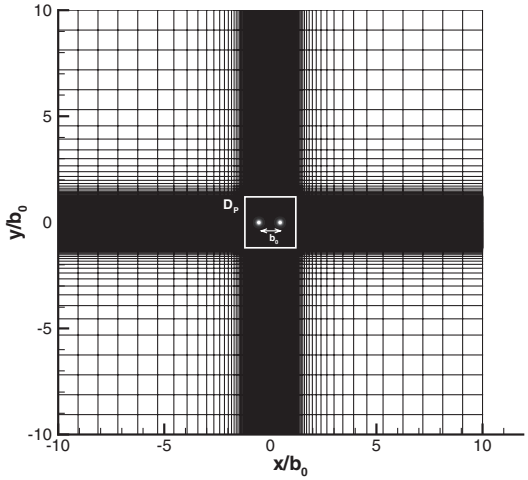

Fig. 1 Computational domain and initial location of the vortex pair. Axes are normalized by the initial spacing b_0 between the vortices.

III. Results

A. Vortex Models and Initial Conditions

The initial velocity field in Eqs. (12–14) consists of a pair of two-dimensional axisymmetric vortices, corotating in the $x - y$ plane. Their properties can be conveniently described by considering an isolated vortex in a cylindrical coordinate system originating at the vortex center (x_c, y_c). In the absence of axial flow the azimuthal velocity v_θ only depends on the radial coordinate r, so that the axial vorticity is given by $\omega = \frac{1}{r}\frac{\partial r v_\theta}{\partial r}$ (for notational ease we skip the symbol $+$ from nondimensional variables). The circulation Γ and the second moment of vorticity Γa^2 are given, respectively, by

$$\Gamma = \int_{-\infty}^{+\infty}\int_{-\infty}^{+\infty} \omega(x, y)\text{d}x\text{d}y = 2\pi\int_0^\infty r\omega(r)\text{d}r \tag{15}$$

$$\Gamma a^2 = \int_{-\infty}^{+\infty}\int_{-\infty}^{+\infty} r^2\omega(x, y)\text{d}x\text{d}y = 2\pi\int_0^\infty r^3\omega(r)\text{d}r \tag{16}$$

where a is the dispersion radius [30]. In incompressible two-dimensional flows these equations identify the basic integral properties of the vortex: Γ is a time invariant and represents the strength of the vortex, and a represents an objective measure of the viscous core size of the vortex as it evolves solely by the effect of viscosity [50,51].

In this study we considered two analytical profiles of v_θ that have been used in the literature to model wake vortices: the LO model and the VM2 model by Fabre and Jacquin [28]. The LO vortex is a classical model with Gaussian distribution of vorticity and azimuthal

velocity given by

$$v_{\mathrm{LO}}(r) = \frac{\Gamma}{2\pi r}(1 - e^{-r^2/a^2}) \tag{17}$$

$$\omega_{\mathrm{LO}}(r) = \frac{\Gamma}{\pi a^2} e^{-r^2/a^2} \tag{18}$$

The relevant length scale is the vortex core radius r_c that identifies the location of maximum velocity $v_c \equiv v_{\mathrm{LO}}(r_c) = \max(v_{\mathrm{LO}})$ (see Fig. 2) and separates the internal region of the vortex with solid body rotation ($v \sim r$) from the external potential-flow region ($v \sim 1/r$). From Eq. (17) it can be easily shown that the core radius is related to the dispersion radius via the relation $1 + 2(r_c^2/a^2) = \exp(r_c^2/a^2)$ or $r_c^2/a^2 \equiv \beta_{\mathrm{LO}} \simeq 1.256$. Finally, integrating Eq. (15) and expressing the circulation in terms of r_c yields

$$\Gamma = 2\pi r_c v_c \alpha_{\mathrm{LO}} \tag{19}$$

with $\alpha_{\mathrm{LO}} \equiv 1/[1 - \exp(-\beta_{\mathrm{LO}})] \simeq 1.398$.

The VM2 model [28] represents the structure of vortex core by means of two length scales, an internal core scale a_1 and an external core scale a_2 (Fig. 2). As in the LO model, the flow is characterized by solid body rotation in the internal core ($r < a_1$) and behaves as potential-flow outside the external core ($r > a_2$). In the intermediate zone $a_1 < r < a_2$ velocity follows a power law $v(r) \sim r^{-\alpha}$. Matching the three laws yields for the azimuthal velocity [28]

$$v_{\mathrm{VM2}}(r) = \frac{\Omega_0 r}{[1 + (r/a_1)^4]^{(1+\alpha)/4}[1 + (r/a_2)^4]^{(1-\alpha)/4}} \tag{20}$$

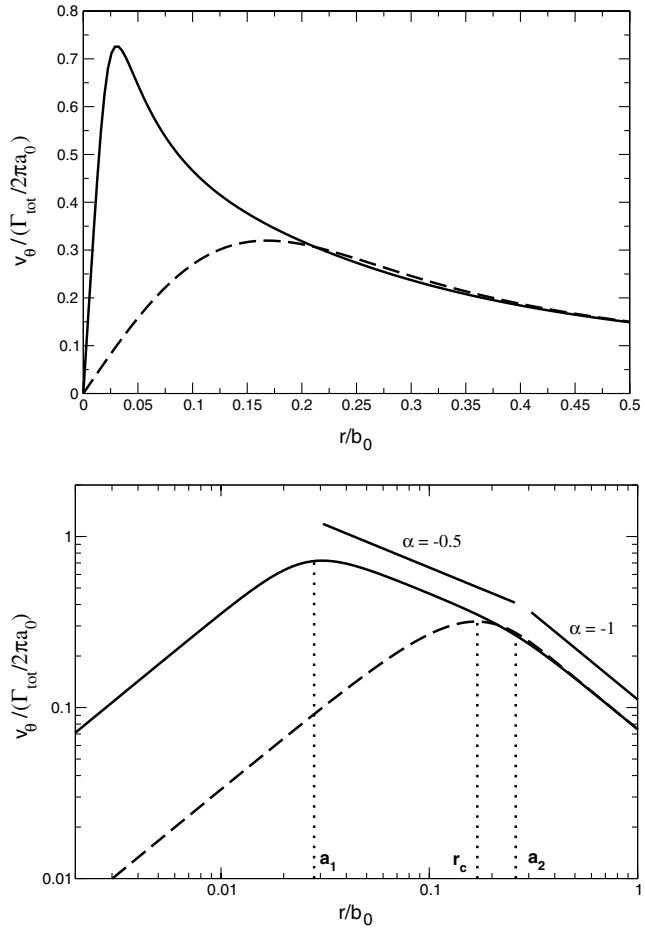

Fig. 2 Initial profiles of the azimuthal velocity of the VM2 (solid line) and LO (dashed line) vortices $a_0/b_0 = 0.15$ (top: linear plot, bottom: logarithmic plot). Profiles are rescaled by the total circulation $\Gamma_{\mathrm{tot}} \equiv 2\Gamma$ and initial dispersion radius a_0; the distance r from the vortex center is normalized by the initial spacing b_0.

$$\omega_{\mathrm{VM2}}(r) = \frac{v_{\mathrm{VM2}}(r)}{r}\left\{2 - \left[\frac{(1+\alpha)a_1}{a_1^4 + r^4} + \frac{(1-\alpha)a_2}{a_2^4 + r^4}\right] r^3\right\} \tag{21}$$

where Ω_0 is the rotation rate of the internal core. Using Eqs. (15) and (21) gives the total circulation $\Gamma = 2\pi\Omega_0 a_1^2 (\frac{a_2}{a_1})^{(1-\alpha)}$. In this study we retained the characteristic parameters $\alpha = 0.5$ and $a_2/a_1 = 10$, as they were found to be representative of aircraft wakes [30]. Using these values and defining the internal $v_1 = \Omega_0 a_1$ and external $v_2 = \Gamma/2\pi a_2$ velocity scales finally yields for the circulation

$$\Gamma = 2\pi v_1 a_1 \alpha_{\mathrm{VM2}}^{0.5,10} \tag{22}$$

with $\alpha_{\mathrm{VM2}}^{0.5,10} \equiv (a_2/a_1)^{1-\alpha} \simeq 3.16$. Inserting Eq. (21) into Eq. (16) and integrating numerically gives the dispersion radius through the relation $a_1^2/a^2 \equiv \beta_{\mathrm{VM2}}^{0.5,10} = 0.0294$.

For the sake of comparison between the two vortex models we choose to conserve the same integral properties Γ and a. Thus, for given LO parameters r_c and v_c, we let a_1 and v_1 be free VM2 parameters and solve for the system:

$$\begin{cases} \frac{a_1^2}{\beta_{\mathrm{VM2}}^{0.5,10}} = \frac{r_c^2}{\beta_{\mathrm{LO}}} \\ 2\pi a_1 v_1 \alpha_{\mathrm{VM2}}^{0.5,10} = 2\pi r_c v_c \alpha_{\mathrm{LO}} \end{cases} \Rightarrow \begin{array}{c} a_1 = \sqrt{\frac{\beta_{\mathrm{VM2}}^{0.5,10}}{\beta_{\mathrm{LO}}}} r_c \simeq 0.153 r_c \\ v_1 = \sqrt{\frac{\beta_{\mathrm{LO}}}{\beta_{\mathrm{VM2}}^{0.5,10}}} \frac{\alpha_{\mathrm{LO}}}{\alpha_{\mathrm{VM2}}^{0.5,10}} v_c \simeq 2.888 v_c \end{array}$$

The initial vortex system is characterized by the ratio a_0/b_0 between the vortex core size a_0 and the vortex spacing b_0. The two values considered here, $a_0/b_0 = 0.1$ and 0.15 (see Table 1), are close to $a/b \sim 0.13$, which was deduced from the experimental results by Jacquin et al. [30] and can be considered as a reasonable estimate in the case of merging between flap and wing-tip aircraft vortices in high-lift configuration. The two vortices have the same circulation and core size, and the total circulation of the system is then $\Gamma_{\mathrm{tot}} \equiv 2\Gamma$.

B. Computational Domain

For both two- and three-dimensional simulations the transverse domain in the xy plane is defined by $L_x = L_y = 20 l_{\mathrm{ref}}$ with a reference length $l_{\mathrm{ref}} \equiv b_0$ (see Fig. 1) and consists of $N_x \times N_y = 401 \times 401$ gridpoints. The computational set-up for various configurations is summarized in Table 1 for convenience. The mesh is regular in the region of interest for the dynamics of the vortex system $D_p = L_{xp} \times L_{yp} = 1.2 b_0 \times 1.2 b_0$ where the grid resolution is $\Delta x_{\mathrm{reg}} = \Delta y_{\mathrm{reg}} = 7 \times 10^{-3} b_0$. For initial ratios $a_0/b_0 = 0.1$ and 0.15 this gives, respectively, 14 and 21 points in the dispersion radius. This resolution was proven to be sufficient to reproduce the main features of the vortex dynamics, as shown by Le Dizès and Laporte [26] and confirmed by Laporte and Leweke [44] in a comparative analysis of numerical simulations and experiments at low a Reynolds number. The mesh is then stretched away to minimize the effects of the borders using a geometric law (see Sec. II.D). The maximum stretching coefficient is $\Delta x_{\max}/\Delta x_{\mathrm{reg}} \simeq 1.23$. In the three-dimensional simulations the transverse domain is

Table 1 Summary of numerical configurations

Run	Model	a/b_0	Re_Γ	Nx	Ny	Nz	L_z/b_0	DNS	LES
L1	LO	0.1	7.5×10^2	401	401	1	0	*	
L2	LO	0.1	1.5×10^3	401	401	1	0	*	
L2b	LO	0.15	1.5×10^3	401	401	1	0	*	
L3	LO	0.1	5.0×10^3	401	401	1	0	*	
L4	LO	0.15	1.0×10^4	401	401	1	0	*	
L5	LO	0.15	1.0×10^4	401	401	36	1.48	*	
L5b	LO	0.15	1.0×10^4	401	401	36	1.92	*	
L6	LO	0.15	2.4×10^5	401	401	36	1.48		*
V1	VM2	0.1	7.5×10^2	401	401	1	0	*	
V2	VM2	0.1	1.5×10^3	401	401	1	0	*	
V3	VM2	0.1	5.0×10^3	401	401	1	0	*	
V4	VM2	0.15	1.0×10^4	401	401	1	0	*	
V5	VM2	0.15	1.0×10^4	401	401	36	1.48	*	
V6	VM2	0.15	2.4×10^5	401	401	36	1.48		*

simply copied in the axial direction, the choice of its extension is discussed in detail in Sec. III.D.

C. Two-Dimensional Stable Merging

The goal of this section is to characterize the basic two-dimensional process of stable merging using DNS and validate our model against theoretical results and available experimental data and correlations [27]; the second goal is to get a reference computational set-up for the three-dimensional simulations of the elliptical instability.

The ensemble of the simulation parameters is reported in Table 1. To illustrate the vortex dynamics during merging we report in Fig. 3 the evolution of the vorticity field for run $L2$, at a Reynolds number based on vortex circulation $Re_\Gamma = \Gamma/\nu = 1.5 \times 10^3$. The figure shows that merging can be decomposed into four stages as first suggested by Cerretelli and Williamson [15]: during the first diffusion stage the vortices simply turn around each other with angular velocity $\Omega_c = \Gamma/\pi b_0^2$ and turnover period $t_c = 2\pi/\Omega_c = 2\pi^2 b_0^2/\Gamma$, while their core size increases by viscous diffusion (Fig. 3a). Although the vortices rapidly become elliptical by mutual stretching, much of their vorticity is confined within the internal separatrix streamline forming an "8-shaped" loop in the reference frame rotating with the vortex system. When some portion of the fluid crosses this separatrix, it is advected along the two external streamlines and the vortices start exchanging their vorticity (Fig. 3b). This sets the beginning of the second stage or convective stage. Filaments of vorticity are created in the two recirculating-flow regions, which ultimately causes vortices to approach each other through the velocity induced by these filaments on each vortex. In the third stage or second diffusion stage, the two vorticity extrema persist until they finally merge (Fig. 3c). During the last stage (axisymmetrization stage), the vorticity filaments reconnect, the vortex axisymmetrizes, and the core size increases by viscous diffusion (Fig. 3d).

It is instructive to analyze the merging process described through the evolution of the dispersion radius $a(t)$ and the vortex spacing $b(t)$, namely the distance between the two vortex centers (identified by local maximum of vorticity) as shown in Fig. 4 for runs $L2$ and $V2$ (note that time is rescaled by the turnover period $t^* = t/t_c$). As pointed out by various authors in the literature [15–17], the onset of the vortex interaction occurs at a critical ratio $(a/b)_c \equiv a(t_1^*)/b(t_1^*)$ at the end of the first diffusion stage (when vortices start to exchange vorticity and $b(t)$ first decreases, see Fig. 4). In all cases considered in this study we obtained $(a/b)_c \equiv a(t_1^*)/b_0 \sim 0.22$, which is independent of Reynolds number and in agreement with the results by Leweke et al. [17]. To evaluate $a(t)$ before merging we used the definition given in Eq. (16) (that is valid for an isolated vortex) and limited the domain of integration to a semi-infinite plane (rotating with the vortex system) that contains one of the vortices and is bounded by the orthogonal line to the vortex separatrix (see Fig. 3a). Note that this technique implicitly assumes that vortices are separated, which is not the case during the third stage of merging (see Fig. 3a), and explains the noisy behavior of $a(t)$ in Fig. 4 for $t_2^* < t^* < t_3^*$. Figure 5 shows the evolution of $b(t)$ and $a(t)$ for various Reynolds numbers and LO initial profiles. In the first stage

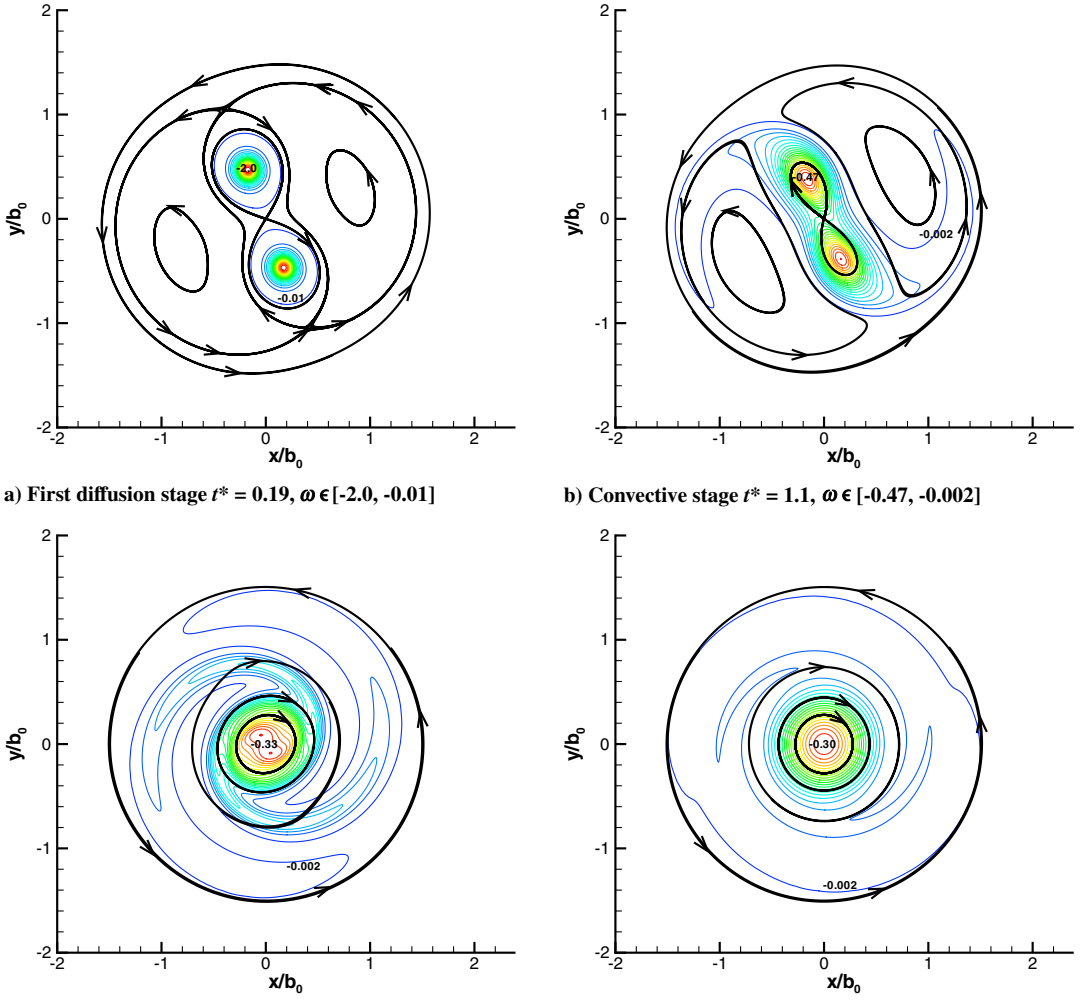

a) First diffusion stage $t^* = 0.19$, $\omega \in [-2.0, -0.01]$

b) Convective stage $t^* = 1.1$, $\omega \in [-0.47, -0.002]$

c) Second diffusion stage $t^* = 1.52$, $\omega \in [-0.33, -0.002]$

d) Axisymmetrization stage $t^* = 2.02$, $\omega \in [-0.3, -0.002]$

Fig. 3 Evolution of the normalized vorticity isocontours $[\omega/(\Gamma/a_0^2)$, 20 levels] during the process of two-dimensional merging (run $V2$). The streamlines are represented by solid black lines and are calculated in the reference frame, rotating at the angular velocity of the vortex system $\Omega = \Gamma/\pi b_0^2$.

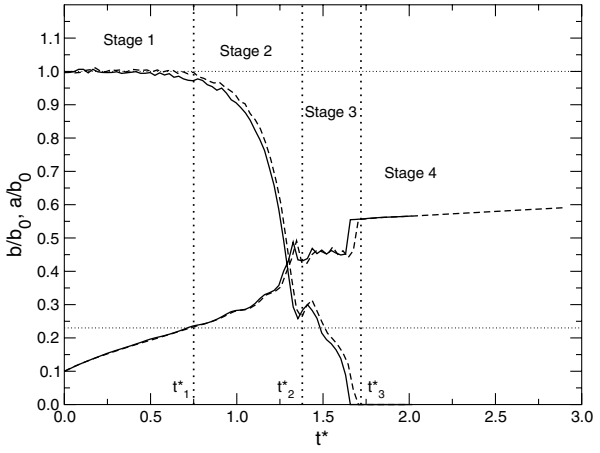

Fig. 4 Evolution of the vortex spacing b and dispersion radius a during two-dimensional merging. The solid lines represent the VM2 initial vortex profile (run $V2$), and the dashed lines represent the LO initial vortex profile (run $L2$). The two falling curves show $b(t)/b_0$, and the two rising curves show $a(t)/b_0$ (b_0 is the initial vortex spacing).

$0 < t^* < t_1^*$ the computed values of a follow the theoretical law valid for an isolated vortex [51]: $a^2(t) = a_0^2 + 4\nu t$. Letting $(a/b)_c \equiv a(t_1^*)/b_0 \sim 0.22$, yields

$$t_1^* = \frac{Re_\Gamma}{8\pi^2}\left[\left(\frac{a}{b}\right)_c^2 - \frac{a_0^2}{b_0^2}\right] \tag{23}$$

During the convective stage, $t_1^* < t^* < t_2^*$, the vortex spacing decreases linearly in time (see Fig. 5) with a rate

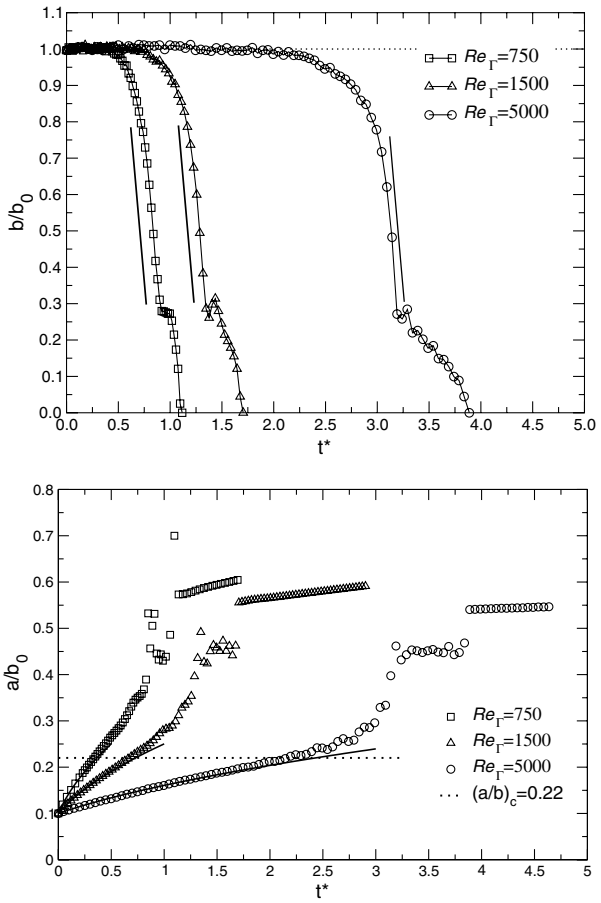

Fig. 5 Evolution of the normalized spacing b/b_0 (top) and dispersion radius a/a_0 (bottom) of an LO vortex for various Re_Γ (symbols). The theoretical diffusion law $a(t) = \sqrt{4\nu t + a_0^2}$ is also represented (solid line).

$\mathrm{d}(b/b_0)/\mathrm{d}t^* = -3.25$, again independent of Reynolds number. During the second diffusion stage, $t_2^* < t^* < t_3^*$, $b(t)$ continues to decrease and attains $b \simeq 0$ at $t = t_3^*$ (which indicates a merging of the vortices). The duration of these two stages are $t_2^* - t_1^* = \text{const} = 0.5$ and $t_3^* - t_2^* = \mathcal{O}(Re^{1/2})$, respectively, and are both in agreement with the results reviewed by Meunier et al. [27].

To analyze the structure of the final merged vortex at $t^* = 1.7$ we reconstructed the tangential velocity profile from the radial circulation profile that is obtained by interpolating the vorticity field on a polar grid originating at the center of the vortex $\omega(x, y) \to \omega(\rho, \theta)$. Integrating on a disk of radius r yields

$$\Gamma(r) = \int_0^{2\pi}\int_0^r \omega(\rho,\theta)\rho\mathrm{d}\rho\mathrm{d}\theta \Rightarrow v_\theta(r) = \frac{\Gamma(r)}{2\pi r} \tag{24}$$

In Fig. 6 we report the evolution of the velocity profiles for run $V2$. The figure shows that the VM2 profile evolves toward a profile described by one length scale because the intermediate region vanishes by diffusion of the internal vortex region (the internal radius a_1 increases while the external radius a_2 remains constant). The velocity profiles become indistinguishable at $t^* \sim 0.66$, just before the beginning of the convective phase [note that this process is faster than complete merging, which is attained at $t^* = 1.7$ (see Fig. 4)]. These results can be associated to the viscous relaxation process identified by Le Dizès and Verga [52]. They demonstrated that two non-Gaussian vortices, such as in the VM2 model, evolve by slow diffusion toward a single attractive solution that corresponds to a Gaussian vortex system as in the LO model. In other words, vortices "forget" the initial two-scale structure before starting to exchange

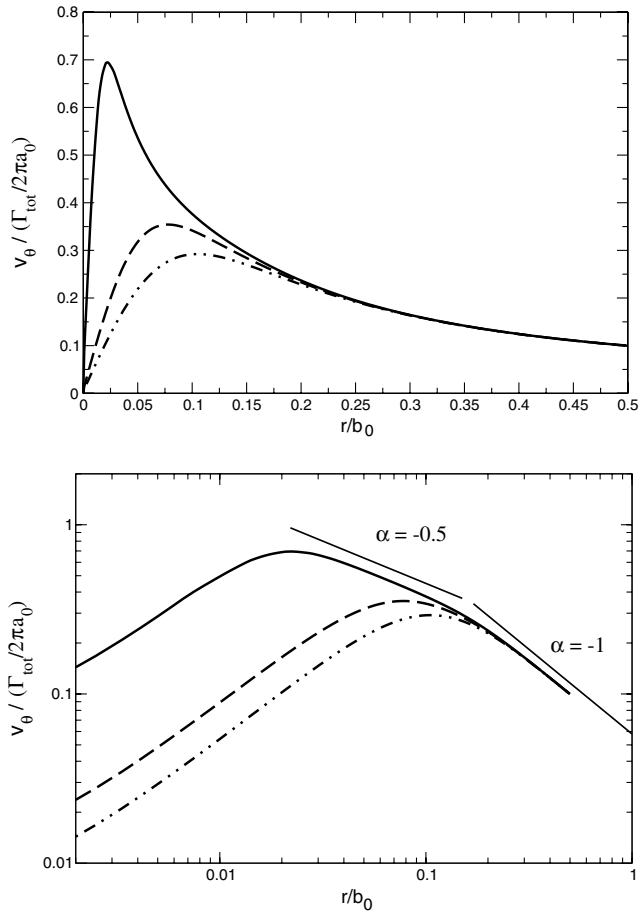

Fig. 6 Evolution of the velocity profiles of a VM2 vortex (run $V2$) where the solid line represents $t^* = 0$, and the dashed line represents $t^* = 0.11$. The dash-dotted line represents $t^* = 0.5$. The top shows a linear plot, and the bottom shows a logarithmic plot. Velocity is rescaled by the total circulation Γ_{tot} of the flow and the initial dispersion radius a_0.

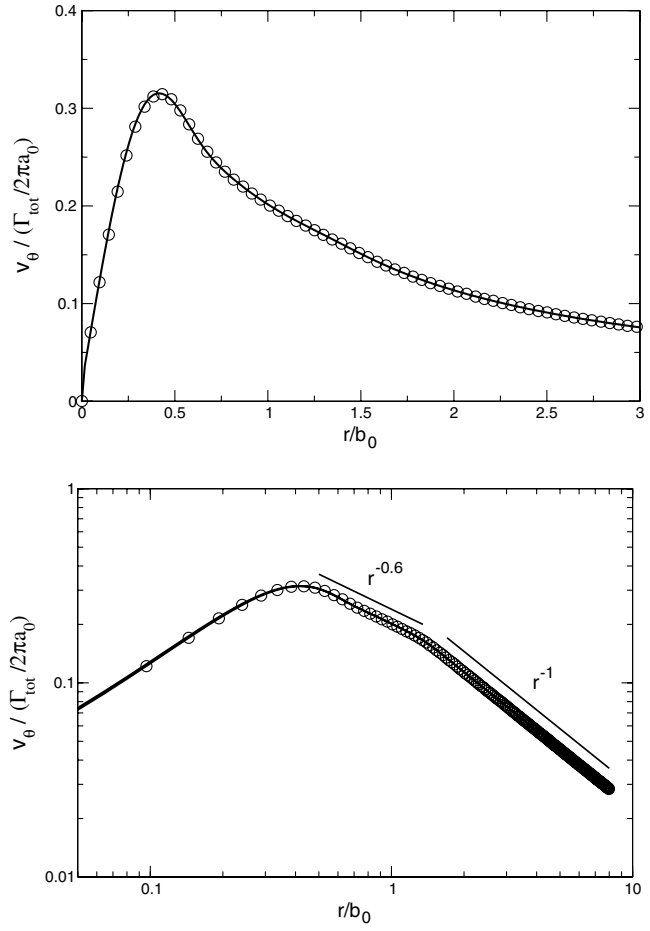

Fig. 7 Velocity profiles of the final merged vortex at $t^* = 1.7$ for the initial VM2 vortex (run *V*2, symbols) and the LO vortex (run *L*2, line). The top shows a linear plot, and the bottom shows a logarithmic plot. Profiles are rescaled by the total circulation Γ_{tot} of the flow and the initial dispersion radius a_0.

their vorticity. At the end of the merging process both models again predict a two-scale vortex structure like in the initial VM2 model but with a steeper power-law region ($\alpha = 0.6$ instead of 0.5). This is clearly shown in the profiles of Fig. 7 that were extracted at $t^* = 1.7$ (runs *L*2 and *V*2) when the final merged vortex has one single core (one vorticity extremum). The same behavior and the same coefficient of the power-law region were obtained for all two-dimensional cases at various (low) Reynolds numbers shown in Table 1, and the behavior was also observed in model-scale experiments by Jacquin et al. [30]. Thus, the two-scale vortex structure seems to be intrinsic to the process of stable merging. The generalization of these results to three-dimensional and high Reynolds number flows is discussed in the next section.

D. Three-Dimensional Unstable Merging

The flow parameters and model equations used for these three-dimensional simulations are again summarized in the Table 1, for both the LO and VM2 vortex pairs. The simulations at $Re_\Gamma = 1.0 \times 10^4$ were chosen for comparison with two-dimensional results of stable merging, although the runs at $Re_\Gamma = 2.4 \times 10^5$ allow flow conditions closer to those encountered in aircraft wakes. The initial condition consists of a corotating vortex pair located at the center of the computational domain as done in Sec. III.C. The theoretical predictions of the elliptical instability by Le Dizès and Laporte [26] were used to determine the mode with the highest growth rate (the most unstable mode) as a function of the flow configuration, Re_Γ and a_0/b_0. In principle, the length of the axial domain L_z can then be chosen as a multiple of the (theoretical) wavelength λ_{ell}^{th} of the elliptical instability; here we took $L_z = 3\lambda_{ell}^{th}$ that ensures the confinement effects of the computational domain are limited [26]. Each wavelength is discretized with 12 points, so that the number of gridpoints in the axial direction is $N_z = 36$. The simplest way to trigger the instability at a given wave number would be to inject energy at the corresponding wavelength using a forcing technique. On the other hand, one motivation of this study was to understand if and how other waves, other than the elliptical instability wave, emerge in corotating vortices. Thus, instead of forcing selectively the elliptical instability, the initial flowfield is perturbed by adding a white noise:

$$\begin{cases} u_0 = u_{\mathrm{LO,VM2}} \times (1 + \varepsilon \mathrm{rand}(x, y, z)) \\ v_0 = v_{\mathrm{LO,VM2}} \times (1 + \varepsilon \mathrm{rand}(x, y, z)) \\ w_0 = 0 \end{cases} \tag{25}$$

where rand $\in [-1/2; 1/2]$ is a random number modeling white noise and $\varepsilon = 10^{-3}$ is the magnitude of the white noise.

1. Topology of the Flow

It has been demonstrated theoretically by Le Dizès and Laporte [26] that a corotating vortex pair can be unstable when the Reynolds number based on circulation is higher than a critical value Re_c that depends on the initial ratio a_0/b_0 (see Fig. 8). Physically, this means that the diffusion of the vortex cores is sufficiently slow that three-dimensional short-wave instability develops when the vortices are still separated (before the convection stage). Figure 8 shows that for $a_0/b_0 = 0.15$ and $Re_c > 3.5 \times 10^3$ all three-dimensional simulations in Table 1 are potentially unstable. We use runs *L*5 and *V*5 to illustrate the three-dimensional dynamics of the vortex system. The short-wave instability is responsible for unstable merging and is shown in Fig. 9 by the sequence of the snapshots of the vorticity magnitude $\|\omega\|$. The development of the instability is characterized by the oscillation of the vortex core in the axial direction (see Fig. 9, $t^* = 1.95$). This form of this oscillation is associated to the most unstable axial mode (i.e., the mode with the highest growth rate, see discussion in Sec. III.D.2). In particular, the figure clearly shows the emergency of mode $k = 4$ for the LO vortex model and mode $k = 3$ for the VM2 vortex model. When the unstable mode saturates, the flow becomes turbulent, and the two vortices start to exchange their vorticity (Fig. 9, $t^* = 2.45$). It can be appreciated from the vorticity isosurfaces that the VM2 vortex simulation exhibits more small-scale turbulent structures than the LO vortex at the same wake age, suggesting that the growth rate of the most unstable mode is higher in the VM2 model so that the instability saturates earlier. This

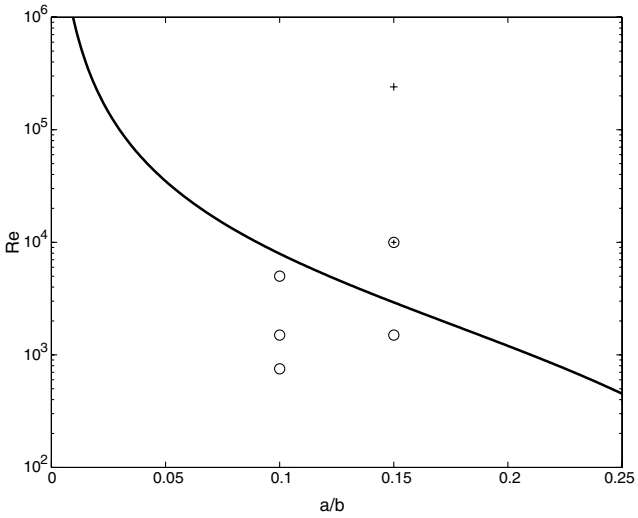

Fig. 8 Theoretical prediction by Le Dizès and Laporte [26] of the critical Reynolds number (Re_c, line) as a function of the ratio a/b for corotating vortices. Symbols correspond to the values of Re_Γ and a_0/b_0 used in the simulations of Table 1: ∘ represents two-dimensional merging, and + represents three-dimensional merging.

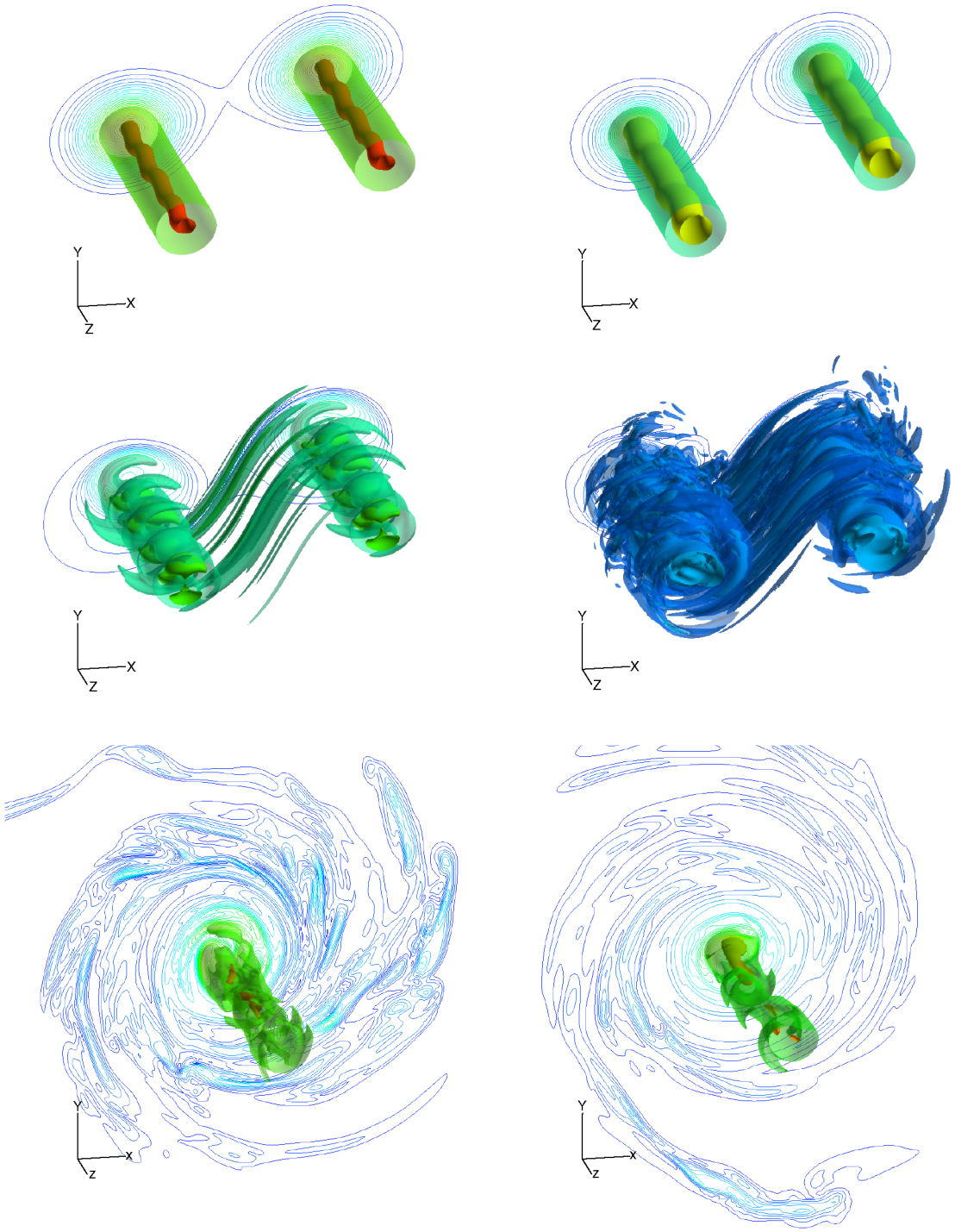

Fig. 9 Evolution of two selected isosurfaces of vorticity magnitude during the unstable merging $\omega_1 = \|\omega\|/(\Gamma/a_0^2) \sim 0.18$ (dark) and $\omega_2 \sim 0.11$ (translucent). The isocontours of the normalized vorticity magnitude are also represented in the first plane (32 levels $\in [\omega_{\min}, \omega_{\max}]$). The left panel shows the initial LO vortex system (run *L5*), and the right panel shows the initial VM2 vortex system (run *V5*). From top to bottom, $t^* = 1.95$, 2.42, and 3.29.

qualitative feature is in good agreement with the linear stability analysis by Fabre and Jacquin [28] and is explained by spectral analysis in Sec. III.D.2. The vortices merge, and the resulting coherent vortex relaminarizes at $t^* = 3.2$. Finally, it is interesting to point out that the development of short-wave instability leads to faster merging compared with the two-dimensional case: for the configuration $a_0/b_0 = 0.15$ and $Re_\Gamma = 1.0 \times 10^4$, the stable merging is reached at about $t^* \sim 5.1$, and the unstable merging is at $t^* \sim 3.2$.

2. *Spectral Analysis*

A spectral analysis was performed by FFT (fast Fourier transform) to determine the effective mode, wavelength, and growth rate of the instability. The growth rate is obtained from the Fourier decomposition of the total kinetic energy

$$\sigma_k = \frac{\mathrm{d}\,\ell n(\widehat{E_k^{1/2}})}{\mathrm{d}t} \tag{26}$$

where $\widehat{E_k^{1/2}}$ is the Fourier coefficient of mode k [24]. The corresponding wavelength is $\lambda_k = \frac{L_z}{k}$ and the wave number is $k_z = \frac{2k\pi}{L_z}$. In all cases a transition is observed before the onset of the instability (which corresponds to the emergence of the dominating unstable mode). The computed growth rates for all three-dimensional runs are reported in Table 2 together with the

Table 2 Spectral analysis results for Fourier mode number k and corresponding instability wavelength λ/b_0 and its growth rate $\sigma^* = \sigma * t_c = \sigma * (2\pi^2 b_0^2/\Gamma)$. The theoretical prediction for Gaussian vortices is also noted, for the viscous configuration $\sigma^*_{\mathrm{th}_v}$ and the inviscid configuration $\sigma^*_{\mathrm{th}_{\mathrm{inv}}}$

Run	k	λ/b_0	σ^*_{num}	$\sigma^*_{\mathrm{th}_v}$	$\sigma^*_{\mathrm{th}_{\mathrm{inv}}}$
L5	4	0.371	5	-	-
L5	3	0.493	3.6	3.47	4.89
L5b	3	0.64	5.1	4.23	5.13
L6	3	0.427	4.6	4.83	4.89
V5	3	0.493	6.2	-	-
V6	7	0.211	6.	-	-

theoretical values obtained from the analysis of linear stability of an LO vortex pair [26].

As mentioned in the previous section the length of the axial domain was taken as 3 times the wavelength of the (theoretical) elliptical instability. However, in run *L5* at $Re_\Gamma = 1.0 \times 10^4$ the most unstable mode obtained from Fourier analysis is $k = 4$ with a wavelength $\lambda_4/b_0 = 0.37$, although the theoretical prediction gives $k = 3$ and $\lambda_3/b_0 = 0.493$. This was qualitatively observed in Fig. 9 and is confirmed in Fig. 10: the mode $k = 3$ develops first, but rapidly saturates before growing again around $t^* \simeq 1.5$ when the mode $k = 4$ emerges as the dominating mode that effectively drives the dynamics of the flow. This mismatch in wave selection is due to the viscosity effects. Indeed, when the vortices start to interact at $t^* \simeq 0.6$ (beginning of the linear regime) their core radius has increased by viscous diffusion to $a(0.6) \simeq 1.19a_0$, and so the effective ratio $a(0.6)/b_0 \simeq 0.178$ is different from the initial $a_0/b_0 = 0.15$ that is used to get the theoretical growth rate. To clarify this point, a second simulation (run *L5b*) was performed with the same initial conditions but with a larger axial domain $L_z/b_0 = 1.92$ that is 3 times the wavelength of the elliptical instability predicted by the theory using $a(0.6)/b_0 = 0.178$ instead of $a_0/b_0 = 0.15$. In this case Fig. 10 shows that mode $k = 3$ emerges as the dominating mode, although with a slightly larger growth rate than the theoretical value (see Table 2).

The aim of run *V5* is to compare the instability occurring in the two vortex models at a relatively low $Re_\Gamma = 1.0 \times 10^4$ and $L_z/b_0 = 1.48$. The spectral analysis indicates that the mode $k = 3$ with $\lambda_3/b_0 = 0.493$ is the most amplified mode, followed by mode $k = 4$ (the opposite of run *L5*). This can be explained by the ratio $a(0.6)/b \simeq 0.178$ and by observing that at the beginning of the linear regime the internal radius a_1 has increased by diffusion $a_1(0.6)/a_1(0) \simeq 1.18$, and external radius is almost the constant $a_2(0.6) \simeq a_2(0)$. On the other hand, Fabre and Jacquin [28] showed that the wavelength of the instability of the VM2 model is of the order of a_1 when the coefficient of the power-law region is $0.5 \leq \alpha < 1$ and of the order of a_2 when $0 < \alpha < 0.4$. At $t^* = 0.6$, α decreased to some value around 0.4 (not shown), so that the results consistently give $\lambda_3 \sim a_2$ as the correct scaling of the instability. Furthermore, for $a_2/a_1 = 10$ and $\alpha = 0.5$ the predicted growth rate of the instability is 30% larger than in an LO model with the same dispersion radius. In run *V5* we obtained $\sigma^*_3 = 6.2$, and in run *L5b* it was $\sigma_3 = 5.1$ (see Table 2), which is consistent considering that the ratio a_2/a_1 slightly decreased at $t^* = 0.6$.

The last two simulations (runs *L6* and *V6*) are useful to compare the flow instability in the two vortex models at $Re_\Gamma = 2.4 \times 10^5$, closer to aircraft wakes Reynolds number. The Fourier analysis shows that mode $k = 3$ is the most amplified mode in the LO model (run *L6*), as expected from linear theory (see Fig. 11). Indeed, as discussed in Sec. III.C for stable merging the dispersion core evolves very slowly at a high Reynolds number so that the initial ratio $a_0/b_0 = 0.15$ is maintained at the beginning of the linear regime. In the case of VM2 vortex profile (run *V6*) the power-law region slightly reduces before the beginning of the linear regime ($t^* \simeq 0.5$). The most amplified mode is $k = 7$, as also reported in Fig. 11. The corresponding wavelength $\lambda_7/b_0 = 0.211$ is closer to the external radius $a_2(0.5)/b_0 \simeq 0.257$ than the internal radius $a_1(0.5)/b_0 \simeq 0.09$, which again is consistent with theoretical prediction [28] because the power-law coefficient $\alpha(0.5)$ is close to 0.4. In addition, the growth rate for VM2 model is higher than the LO model (see Table 2).

3. *Structure of the Final Vortex*

An important question we want to address in this study is whether the different growth rates of the instability, associated with the different vortex models and flow conditions, reflect into different profiles of the final merged vortex. This is also critical information that is needed to characterize the counter-rotating vortex pair in the extended near-field wake and to quantify the wake hazard in the following far-field wake. To extract the velocity profiles of the final merged vortex at $t^* = 3.93$, we averaged the velocity fields in the axial direction and interpolated these fields into a polar grid as done in Sec. III.C [see Eq. (24)]. These profiles are plotted in Fig. 12 for runs *L5*, *V5* and *L6*, *V6*. It is interesting to observe that all curves exhibit two-scale vortex profile as in the VM2 model. The coefficient of the power-law region is roughly the same for all cases analyzed, $\alpha \sim 0.35 - 0.4$ (although it is different from the value $\alpha = 0.5$ used to initialize VM2 runs). According to the findings mentioned earlier, we can reasonably conclude that the structure of the merged vortex seems to be independent of Reynolds numbers and the initial conditions (vortex profile and ratio a/b), but it depends on the type (stable or unstable) of merging. Indeed, in the case of stable merging

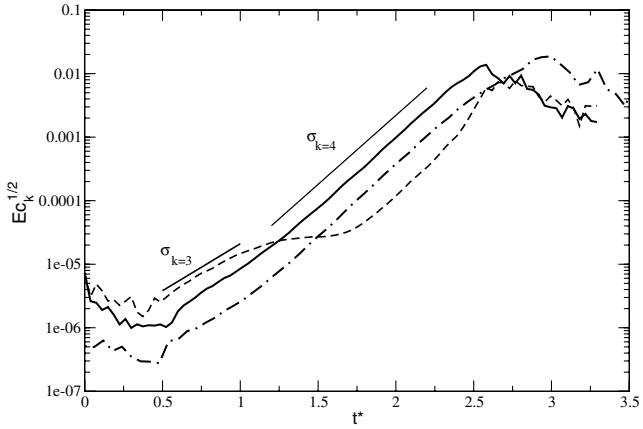

Fig. 10 Time history of the energy of the most unstable Fourier modes (runs *L5* and *L5b*). The solid line represents $L_z/b_0 = 1.48$ and $k = 3$, and the dashed line represents $L_z/b_0 = 1.48$ and $k = 4$. The dashed-dot line represents $L_z/b_0 = 1.92$ and $k = 3$.

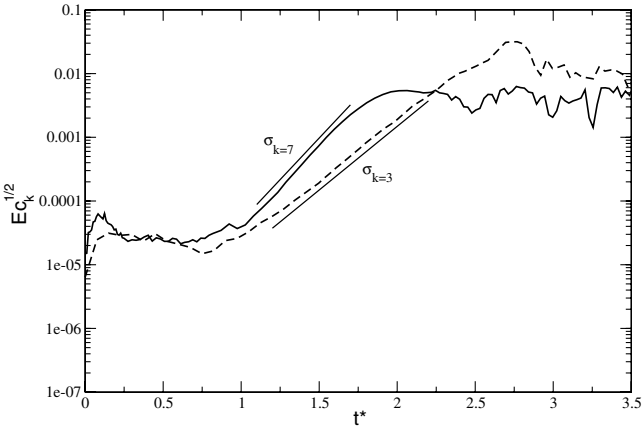

Fig. 11 Time history of the energy of the most unstable Fourier modes at a high Reynolds number $Re_\Gamma = 2.4 \times 10^5$. The dashed line represents the initial LO vortex (run *L6*), and the solid line represents the initial VM2 vortex (run *V6*).

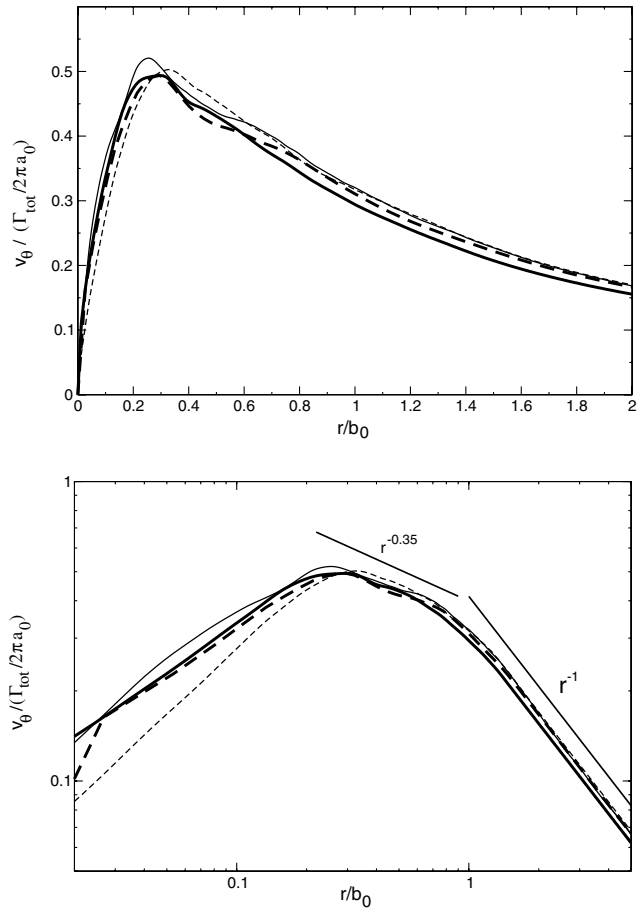

Fig. 12 Velocity profiles of the final vortex at the end of unstable merging. The top shows a linear plot, and the bottom shows a logarithmic plot. The dashed lines represent the initial LO vortex (runs *L*5 and *L*6), and the solid lines represent the initial VM2 vortex (runs *V*5 and *V*6). The thick lines represent $t^* = 3.29$ and $Re_\Gamma = 1.0 \times 10^4$, and the thin lines represent $t^* = 3.93$ for $Re_\Gamma = 2.4 \times 10^5$.

we obtained $\alpha \simeq 0.6$ in the power-law region in all cases considered here (runs $L1 \rightarrow L4$ and $V1 \rightarrow V4$).

IV. Conclusions

In this work we used direct and large-eddy simulation to analyze the process of stable and unstable merging of corotating vortices and its dependence on the initial vortex profile, vortex spacing, and Reynolds number. In the two-dimensional stable case, DNS at various low Reynolds numbers showed that merging is initiated by the exchange of vorticity between the vortices, which is favored by the viscous diffusion of the cores and is associated to a critical ratio of vortex dispersion radius over vortex spacing $(a/b)_c \sim 0.22$, in accordance with literature work. The results showed that Reynolds number does not affect the dynamics of the flow and the structure of the final merged vortex but increases the final time of merging. The three-dimensional, unstable merging was simulated using direct and large-eddy simulations for Reynolds numbers ranging from $Re_\Gamma = 1.0 \times 10^4$ to 2.4×10^5. The results showed that the elliptical instability develops in the vortex core due to the strain field, which is induced by one vortex on the other. The computed growth rates agree with the theoretical predictions both for the one-scale vortex pair (LO model) and the two-scale vortex pair (VM2 model), provided the correct development of the vortex core size is taken into account in the wave selection of the elliptical instability. It was found that the growth rate of instability is higher in a VM2 model than an LO model, although the profile of tangential velocity is the same. This seems to be a common feature of stable and unstable merging: the structure of the final vortex is independent of the Reynolds number and the initial ratio a_0/b_0 and is characterized by a two-scale vortex velocity profile. However, the coefficient α of the power-law region $r^{-\alpha}$ does depend on the type of merging: for a stable merging $\alpha \sim 0.6$ and in the other case $\alpha \sim 0.35$.

Acknowledgments

Financial support was provided by the European project FAR-Wake (Fundamental Research on Aircraft Wake Phenomena), under contract AST-CT-2005-012238. The authors wish to thank H. Moet for helpful discussions.

References

[1] Jimenez, J., Moffatt, H. K., and Vasco, C., "The Structure of Vortices in Freely Decaying Two-Dimensional Turbulence," *Journal of Fluid Mechanics*, Vol. 313, April 1996, pp. 209–222. doi:10.1017/S0022112096002182

[2] Vincent, A., and Meneguzzi, M., "The Spatial Structure and Statistical Properties of Homogeneous Turbulence," *Journal of Fluid Mechanics*, Vol. 225, April 1991, pp. 1–20. doi:10.1017/S0022112091001957

[3] Provenzale, A., "Transport by Coherent Barotropic Vortices," *Annual Review of Fluid Mechanics*, Vol. 31, No. 1, 1999, pp. 55–93. doi:10.1146/annurev.fluid.31.1.55

[4] Rossow, V. J., "Lift-Generated Vortex Wakes of Subsonic Transport Aircraft," *Progress in Aerospace Sciences*, Vol. 35, No. 6, 1999, pp. 507–660. doi:10.1016/S0376-0421(99)00006-8

[5] Gerz, T., Holzäpfel, F., and Darracq, D., "Commercial Aircraft Wake Vortices," *Progress in Aerospace Sciences*, Vol. 38, No. 3, 2002, pp. 181–208. doi:10.1016/S0376-0421(02)00004-0

[6] Spalart, P., "Airplane Trailing Vortices," *Annual Review of Fluid Mechanics*, Vol. 30, No. 1, 1998, pp. 107–138. doi:10.1146/annurev.fluid.30.1.107

[7] Crouch, J., and Jacquin, L., "Aircraft Trailing Vortices," *Comptes Rendus Physique*, Vol. 6, Nos. 4–5, 2005, pp. 487. doi:10.1016/j.crhy.2005.05.006

[8] Green, G. C., "An Approximated Model of Vortex Decay in the Atmosphere," *Journal of Aircraft*, Vol. 23, No. 7, 1986, pp. 566–573. doi:10.2514/3.45345

[9] Corjon, A., and Poinsot, T., "Vortex Model to Define Safe Aircraft Separation Standards," *Journal of Aircraft*, Vol. 33, No. 3, 1996, pp. 547–553. doi:10.2514/3.46979

[10] Sarpkaya, T., "New Model for Vortex Decay in the Atmosphere," *Journal of Aircraft*, Vol. 37, No. 1, 2000, pp. 53–61. doi:10.2514/2.2561

[11] Sarpkaya, T., Robins, R. E., and Delisi, D. P., "Wake-Vortex Eddy-Dissipation Model Predictions Compared with Observations," *Journal of Aircraft*, Vol. 38, No. 4, 2001, pp. 687–692. doi:10.2514/2.2820

[12] Holzäpfel, F., "Probabilistic Two-Phase Wake Vortex Decay and Transport Model," *Journal of Aircraft*, Vol. 40, No. 2, 2003, pp. 323–331. doi:10.2514/2.3096

[13] Holzäpfel, F., and Robins, R. E., "Probabilistic Two-Phase Aircraft Wake-Vortex Model: Application and Assessment," *Journal of Aircraft*, Vol. 41, No. 5, 2004, pp. 1117–1126. doi:10.2514/1.2280

[14] Holzäpfel, F., "Probabilistic Two-Phase Aircraft Wake Vortex Model: Further Development and Assessment," *Journal of Aircraft*, Vol. 43, No. 3, 2006, pp. 700–708. doi:10.2514/1.16798

[15] Cerretelli, C., and Williamson, C. H. K., "The Physical Mechanism for Vortex Merging," *Journal of Fluid Mechanics*, Vol. 475, Jan. 2003, pp. 41–77. doi:10.1017/S0022112002002847

[16] Meunier, P., Ehrenstein, U., Leweke, T., and Rossi, M., "A Merging Criterion for Two-Dimensional Corotating Vortices," *Physics of Fluids*, Vol. 14, No. 8, 2002, pp. 2757–2766. doi:10.1063/1.1489683

[17] Leweke, T., Meunier, P., Laporte, F., and Darracq, D., "Controlled Interaction of Co-Rotating Vortices," *3rd ONERA-DLR Aerospace Symposium*, Paper S2-3, ONERA, Paris, 2001.

[18] Ferreira de Sousa, P. J. S. A., and Pereira, J. C. F., "Reynolds Number

Dependence of Two-Dimensional Laminar Co-Rotating Vortex Merging," *Theoretical and Computational Fluid Dynamics*, Vol. 19, No. 1, 2005, pp. 65–75.
doi:10.1007/s00162-004-0154-0

[19] Orlandi, P., "Two-Dimensional and Three-Dimensional Direct Numerical Simulation of Co-Rotating Vortices," *Physics of Fluids*, Vol. 19, No. 1, 2007, pp. 1–18.
doi:10.1063/1.2424498

[20] Moore, D. G., and Saffman, P. G., "The Instability of a Straight Vortex Filament in a Strain Field," *Proceedings of the Royal Society of London. Series A, Mathematical and Physical Sciences*, Vol. A346, No. 1646, 1975, pp. 413–425.
doi:10.1098/rspa.1975.0183

[21] Kerswell, R. R., "Elliptical Instability," *Annual Review of Fluid Mechanics*, Vol. 34, 2002, pp. 83–113.
doi:10.1146/annurev.fluid.34.081701.171829

[22] Crow, S. C., "Stability Theory for a Pair of Trailing Vortices," *AIAA Journal*, Vol. 8, No. 12, 1970, pp. 2172–2179.
doi:10.2514/3.6083

[23] Leweke, T., and Williamson, C. H. K., "Cooperative Elliptic Instability of a Vortex Pair," *Journal of Fluid Mechanics*, Vol. 360, April 1998, pp. 85–119.
doi:10.1017/S0022112097008331

[24] Laporte, F., and Corjon, A., "Direct Numerical Simulations of the Elliptic Instability of a Vortex Pair," *Physics of Fluids*, Vol. 12, 2000, pp. 1016–1031.
doi:10.1063/1.870357

[25] Meunier, P., and Leweke, T., "Three-Dimensional Instability During Vortex Merging," *Physics of Fluids*, Vol. 13, No. 10, 2001, pp. 2747–2750.
doi:10.1063/1.1399033

[26] Le Dizès, S., and Laporte, F., "Theoretical Prediction for Elliptical Instability in a Two-Vortex Flow," *Journal of Fluid Mechanics*, Vol. 471, Nov. 2002, pp. 169–201.
doi:10.1017/S0022112002002185

[27] Meunier, P., Le Dizès, S., and Leweke, T., "Physics of Vortex Merging," *Comptes Rendus. Physique*, Vol. 6, Nos. 4–5, 2005, pp. 431–450.
doi:10.1016/j.crhy.2005.06.003

[28] Fabre, D., and Jacquin, L., "Short-Wave Cooperative Instabilities in Representative Aircraft Vortices," *Physics of Fluids*, Vol. 16, No. 5, 2004, pp. 1366–1378.
doi:10.1063/1.1686951

[29] Devenport, W. J., Riffe, M. C., Liapis, S. I., and Follin, G. J., "The Structure and Development of a Wing-Tip Vortex," *Journal of Fluid Mechanics*, Vol. 312, April 1996, pp. 67–106.
doi:10.1017/S0022112096001929

[30] Jacquin, L., Fabre, D., Geffroy, P., and Coustols, E., "The Properties of a Transport Aircraft Wake in the Extended Near Field: An Experimental Study," *39th AIAA Aerospace Sciences Meeting and Exhibit*, AIAA Paper 2001-1038, 2001.

[31] Hirschfelder, J. O., Curtiss, C. F., and Bird, R. B., *Molecular Theory of Gases and Liquids*, Wiley, New York, 1964, p. 1249.

[32] Erlebacher, G., Hussaini, M. Y., Speziale, C. G., and Zang, T. A., "Towards the Large-Eddy Simulation of Compressible Turbulence," *Journal of Fluid Mechanics*, Vol. 238, May 1992, pp. 155–185.
doi:10.1017/S0022112092001678

[33] Lesieur, M., and Comte, P., "Favre Filtering and Macro-Temperature in Large-Eddy Simulations of Compressible Turbulence," *Comptes Rendus de l'Académie des Sciences. Série IIb*, Vol. 329, No. 5, 2001, pp. 363–368.
doi:10.1016/S1620-7742(01)01331-9

[34] Yoshizawa, A., "Statistical Theory for Compressible Turbulent Shear Flows, with the Application to Subgrid Modeling," *Physics of Fluids A*, Vol. 29, No. 7, 1986, pp. 2152–2164.
doi:10.1063/1.865552

[35] Ng, L., and Erlebacher, G., "Secondary Instabilities in Compressible Boundary Layers," *Physics of Fluids A*, Vol. 4, No. 4, 1992, pp. 710–726.
doi:10.1063/1.858290

[36] Gerz, T., and Holzäpfel, F., "Wing-Tip Vortices, Turbulence and the Distribution of Emissions," *AIAA Journal*, Vol. 37, No. 10, 1999, pp. 1270–1276.
doi:10.2514/2.595

[37] Moin, P., Squires, K., Cabot, W., and Lee, S., "A Dynamic Subgrid-Scale Model for Compressible Turbulence and Scalar Transport," *Physics of Fluids A*, Vol. 3, Nov. 1991, pp. 2746–2757.
doi:10.1063/1.858164

[38] Pitsch, H., and Steiner, S., "Large-Eddy Simulation of a Turbulent Piloted Methane/Air Diffusion Flame (Sandia Flame D)," *Physics of Fluids*, Vol. 12, No. 10, 2000, pp. 2541–2554.
doi:10.1063/1.1288493

[39] Métais, O., and Lesieur, M., "Spectral Large-Eddy Simulation of Isotropic and Stably Stratified Turbulence," *Journal of Fluid Mechanics*, Vol. 239, No. 1, 1992, pp. 157–194.
doi:10.1017/S0022112092004361

[40] Ducros, F., Comte, P., and Lesieur, M., "Large-Eddy Simulation of Transition to Turbulence in a Boundary Layer Spatially Developing over a Flat Plate," *Journal of Fluid Mechanics*, Vol. 326, Nov. 1996, pp. 1–36.
doi:10.1017/S0022112096008221

[41] Cocle, R., Dufresne, L., and Winckelmans, G., "Investigation of Multiscale Subgrid Models for LES of Instabilities and Turbulence in Wake Vortex Systems," *Complex Effects in Large Eddy Simulation, Lecture Notes in Computational Science and Engineering*, Springer–Verlag, New York, 2007, pp. 141–160.

[42] Stoessel, A., "An Efficient Tool for the Study of 3D Turbulent Combustion Phenomena on MPP Computers," *Proceedings of the HPCN 95 Conference*, Springer, Milan, 1995, pp. 306–311.

[43] Gamet, L., Ducros, F., Nicoud, F., and Poinsot, T., "Compact Finite Difference Schemes on Non-Uniform Meshes. Application to Direct Numerical Simulations of Compressible Flows," *International Journal for Numerical Methods in Fluids*, Vol. 29, No. 2, 1999, pp. 159–191.
doi:10.1002/(SICI)1097-0363(19990130)29:2<159::AID-FLD781>3.0.CO;2-9

[44] Laporte, F., and Leweke, T., "Elliptic Instability of Counter-Rotating Vortices: Experiment and Direct Numerical Simulation," *AIAA Journal*, Vol. 40, No. 12, 2002, pp. 2483–2494.
doi:10.2514/2.1592

[45] Paoli, R., Laporte, F., Cuénot, B., and Poinsot, T., "Dynamics and Mixing in Jet/Vortex Interactions," *Physics of Fluids*, Vol. 15, No. 7, 2003, pp. 1843–1860.
doi:10.1063/1.1575232

[46] Paoli, R., Hélie, J., and Poinsot, T., "Contrail Formation in Aircraft Wakes," *Journal of Fluid Mechanics*, Vol. 502, March 2004, pp. 361–373.
doi:10.1017/S0022112003007808

[47] Moet, H., Laporte, F., Chevalier, G., and Poinsot, T., "Wave Propagation in Vortices and Vortex Bursting," *Physics of Fluids*, Vol. 17, No. 5, 2005, pp. 1–15.
doi:10.1063/1.1896937

[48] Lele, S. K., "Compact Finite Difference Scheme with Spectral-Like Resolution," *Journal of Computational Physics*, Vol. 103, No. 1, 1992, pp. 16–42.
doi:10.1016/0021-9991(92)90324-R

[49] Ragab, S., and Sreedhar, M., "Numerical Simulation of Vortices with Axial Velocity Deficits," *Physics of Fluids*, Vol. 7, March 1995, pp. 549–558.
doi:10.1063/1.868582

[50] Ting, L., and Klein, R., *Viscous Vortical Flows: Lecture Notes in Physics*, Vol. 374, Springer-Verlag, New York, 1991.

[51] Saffman, P. G., *Vortex Dynamics*, Cambridge Univ. Press, Cambridge, England, U.K., 1992.

[52] Le Dizès, S., and Verga, A., "Viscous Interactions of Two Co-Rotating Vortices Before Merging," *Journal of Fluid Mechanics*, Vol. 467, Sept. 2002, pp. 389–410.
doi:10.1017/S0022112002001532

S. Fu
Associate Editor